Published in final edited form as:
Biochemistry. 2006 September 5; 45(35): 10729–10738. doi:10.1021/bi060893t.

Mechanistic studies on the mononuclear Zn(II)-containing metallo-β-lactamase ImiS from *Aeromonas sobria*†

Narayan P. Sharma‡, **Christine Hajdin**‡, **Sowmya Chandrasekar**‡, **Brian Bennett**§, **Ke-Wu Yang**‡, and **Michael W. Crowder**‡,*

‡ *Department of Chemistry and Biochemistry, 112 Hughes Hall, Miami University, Oxford, OH 45056*

§ *National Biomedical EPR Center, Department of Biophysics, Medical College of Wisconsin, 8701 Watertown Plank Road, Milwaukee, WI 53226-0509*

Abstract

In an effort to understand the reaction mechanism of a B2 metallo-β-lactamase, steady-state and pre-steady state kinetic and rapid-freeze quench EPR studies were conducted on ImiS and its reaction with imipenem and meropenem. pH Dependence studies revealed no inflection points in the pH range of 5.0 – 8.5, while proton inventories demonstrated at least 1 rate-limiting proton transfer. Site-directed mutagenesis studies revealed that Lys224 plays a catalytic role in ImiS, while the side chain of Asn233 does not play a role in binding or catalysis. Stopped-flow fluorescence studies on ImiS, which monitor changes in tryptophan fluorescence on the enzyme, and its reaction with imipenem and meropenem revealed biphasic fluorescence time courses with a rate of fluorescence loss of 160 s^{-1} and a slower rate of fluorescence regain of 98 s^{-1}. Stopped-flow UV-Vis studies, which monitor the concentration of substrate, revealed a rapid loss in absorbance during catalysis with a rate of 97 s^{-1}. These results suggest that the rate-limiting step in the reaction catalyzed by ImiS is C-N bond cleavage. Rapid-freeze quench EPR studies on Co(II)-substituted ImiS demonstrated the appearance of a rhombic signal after 10 milliseconds that is assigned to a reaction intermediate that has a 5-coordinate metal center. A distinct product (EP) complex was also observed and began to appear in 18–19 milliseconds. Taken together, these results allow for a reaction mechanism to be offered for the B2 metallo-β-lactamases and demonstrates that the mononuclear Zn(II)- and dinuclear Zn(II)-containing enzymes share a common rate-limiting step, which is C-N bond cleavage.

Bacterial resistance to antibiotics is a growing clinical concern (1,2). Zn(II)-containing β-lactamases (metallo-β-lactamases, MβL's) contain 1–2 moles of Zn(II) per mole of enzyme, hydrolyze all known cephalosporins, carbapenems and penicillins, are not inhibited by clavulanic acid and other classical β-lactamase inhibitors, and have no known clinically-useful inhibitor towards them (3,4). Previous studies have shown that there is significant structural and mechanistic diversity among the MβL's, leading to the grouping of the enzymes into three distinct subclasses: B1, B2, and B3 (5,6). Sequence identity ranges from 25–40% between members in one subclass and from 10–20% between members in different subclasses. Subclass B1 enzymes have been found in strains of *Bacillus*, *Bacteroides*, *Pseudomonas*, *Serratia*, and *Chryseobacterium*, and subclass B3 enzymes have been found in strains of *Stenotrophomonas*, *Legionella*, *Fluoribacter*, *Janthinobacterium* and *Caulobacter* (3,4). Enzymes from the B1 and B3 subclasses have broad substrate profiles and require two Zn(II)

†This work was supported by the National Institutes of Health (GM40052 to MWC; AI056231 to BB, and EB001980 to the Medical College of Wisconsin).

*To whom correspondence should be addressed: M. W. Crowder, e-mail: crowdemw@muohio.edu, phone: (513) 529-7274, fax: (513) 529-5715.

ions for maximal enzymatic activity (3). In contrast, subclass B2 enzymes have a relatively narrow substrate profile, hydrolyzing carbapenems almost exclusively (3) and exhibit maximal activity when bound to only 1 Zn(II) (7). In fact, the binding of a second Zn(II) ion is inhibitory (7). These carbapenemases are produced by various species of *Aeromonas*. Aeromonads are enteric, anaerobic, Gram-negative pathogens that cause a range of symptoms from mild diarrhea to acute gastroenteritis in humans (8), and *Aeromonas* species have been found in wound infections (9). One alarming characteristic of Aeromonads is that they are water-borne and typically are present in purified, drinking water (10). To date there is no crystal structure available for ImiS, but the crystal structure of another subclass B2 enzyme, CphA from *Aeromonas hydrophila*, has been recently reported (11). This structure showed Zn(II) bound to His263, Cys221, Asp120, and a water; this site is the consensus Zn_2 site in MβL's (3). Recent spectroscopic studies have demonstrated that Zn(II)/Co(II) preferentially binds to this same site in ImiS (12). Previous biochemical, kinetic, and inhibition studies have suggested significant structural and mechanistic differences among the different group B β-lactamases (3,4,13). These results suggest that one inhibitor may not be effective in treating all infections caused by bacteria that produce a metallo-β-lactamase. Toney and Moloughney recently reviewed the literature on inhibitors of MβL's (13), and most of these inhibitors are effective against only one or two of the enzymes. This is not surprising since, with few exceptions (14–16), the design of most of the inhibitors was guided by studies on only one enzyme. To address this problem, we are currently characterizing a metallo-β-lactamase from each of the group B subclasses (CcrA, ImiS, and L1) in an effort to identify common structural/mechanistic properties of the enzymes towards which a single inhibitor can be designed. While extensive mechanistic studies have been reported on B1 and B3 MβL's (17–24), there is little known about the mechanism of a B2 MβL. Herein, we describe the first detailed mechanistic studies on a B2 MβL, specifically ImiS from *A. veronii bv. sobria.*

Experimental Procedures

Preparation of ImiS samples

Recombinant ImiS was prepared as described previously (25). Briefly, the over-expression plasmid, pET26b-ImiS, was used to transform BL21(DE3) *Escherichia coli* cells. A 10 mL overnight culture of these cells in LB (Luria-Bertani) medium was used to innoculate 4 × 1 L of LB medium containing 25 μg/mL kanamycin and 29 μg/mL $ZnSO_4{\cdot}7H_2O$. The cells were allowed to grow at 37 °C with shaking until the cells reached an optical density at 600 nm of 0.6–0.8. Protein production was induced with 1 mM isopropyl-β-*D*-thiogalactopyranoside (IPTG), and the cells were shaken at 37 C for 3 h. The cells were collected by centrifugation (15 min at 7000 xg) and resuspended in 30 mL of 50 mM Tris, pH 7.0, containing 500 mM NaCl. The cells were ruptured by two passages through a French press at 16,000 lb/in., and the cell debris was separated by centrifugation (30 min at 25000 ×g). The cleared supernatant was dialyzed versus 2L of 50 mM Tris, pH 7.0, overnight at 4 C, centrifuged to remove insoluble matter, and loaded onto a SP-Sepharose column (1.5 × 12 cm with 25 mL bed volume) that was equilibrated with 50 mM Tris, pH 7.0. Bound proteins were eluted with a 0 to 500 mM NaCl gradient in 50 mM Tris, pH 7.0, at 2 mL/min. Fractions (8 mL) containing ImiS were pooled and concentrated with an Amicon ultrafiltration cell equipped with a YM-10 membrane. Protein purity was ascertained by sodium dodecyl sulfate (SDS) polyacrylamide gel electrophoresis. ImiS concentrations were determined using Beer's Law and an extinction coefficient of 37,250 $M^{-1}cm^{-1}$ (25). Co(II)-substituted ImiS was prepared as previously described (12).

Substrate Inhibition Studies

Substrate inhibition studies were carried out on recombinant ImiS using imipenem or meropenem as substrate. Assays were conducted at 25°C in 50 mM Tris, pH 7.0, on an HP

5480A diode array UV-Visible spectrophotometer. Initial velocity versus imipenem concentration data were plotted and fitted with Michaelis-Menten equations assuming different modes of substrate inhibition (26). Imipenem and meropenem were gifts from Merck & Co. (Rahway, NJ) and Zeneca Pharmaceuticals (Wilmington, DE), respectively.

Product studies

Hydrolyzed products of imipenem were prepared by incubating 8 mM imipenem in 50 mM Tris, pH 7.0, with either 190 μM ImiS or 100 μM L1 (27), and the reactions were incubated on ice for 2 hours. The enzymes were removed by using ultrafiltration (Centricon-10), and the resulting product containing solutions were analyzed at 280 and 300 nm using UV-Vis spectrophotometry to determine whether the solutions contained any protein or unhydrolyzed imipenem. The solutions were then flash frozen in liquid nitrogen and lyophilized overnight. The products were analyzed with ^{1}H NMR spectroscopy (Bruker 500 MHz) or by LC-MS (Bruker Esquire, ESI). The lyophilized products were then dissolved in 50 mM Tris, pH 7.0, and used in product inhibition studies with L1 (nitrocefin as substrate) and ImiS (imipenem as substrate).

pH Dependence studies

pH Dependence studies were performed on recombinant ImiS over the pH range of 5.0–8.5 using a multicomponent buffer, MTEN. MTEN (25 mM MES, 25 mM Tris, 25 mM ethanolamine, and 100 mM NaCl) was used to minimize the effects of using different buffers over wide ranges of pH, and the NaCl was included to normalize the ionic strength effects in the buffer (28). The pH of the buffers was ascertained by using a pH meter. Steady-state kinetic assays were conducted at 25 C in 50 mM Tris buffer, pH 7.0, on a HP 5480 diode array UV-visible spectrophotometer. Steady-state kinetic constants, K_M and k_{cat}, were determined by fitting initial velocity versus substrate concentration data directly to the Michaelis-Menten equation using Igor Pro v. 4.0.5.1 (Wavemetrics). The pH dependence data were fitted with Leonara (29); however, no pK_a values above 5.5 or below 8 were revealed with this software.

Proton Inventories

Proton inventories were performed with ImiS in MTEN buffer, pH/pD = 7.0, using imipenem as the substrate. Enzyme and substrate were incubated in the D_2O containing buffer for 30 minutes to allow full proton-deuteron equilibration. Data were collected in buffers containing 0, 25, 50, 75, and 100 % D_2O (mole fraction of D_2O (n) = 0, 0.25, 0.5, 0.75, and 1.0). The steady-state kinetic constant, $k_{cat,}$ was obtained as described above. The resulting kinetic constants were plotted versus their mole fraction D_2O and fitted to the Gross-Butler equation for one ($k_{cat0}[1-n+(n*(k^D/k^H))]$, two ($k_{cat0}[1-n+(n*(k^D/k^H)][1-n+n*(k^D/k^H)]$, and multiple ($k_{cat\ 0}[(k^D/k^H)^n]$) protons in flight models (30,31).

Generation and Characterization of K224T and N233S Mutants

By using the PAGE-purified oligonucleotides primers and the over-expression plasmid for ImiS (pET26b-ImiS) as the template, ImiS mutants were generated using the Quikchange Site-Directed mutagenesis kit according to manufacturer's instructions. The primers used for the mutagenesis studies were: K224TFor, CTTTATggCAACTgCATCCTCACCgAGAAGCTgggCAACCTgAgCTTTgCC; K224TRev, ggCAAAgCTCAggTTgCCCAgCTTCTCggTgAggATgCAgTTgCCATAAAg; N223SFor, gCCTTCACATCggCAAAgCTCAggCTgCCCAgCTTCTCCTTgAggAT; N223SRev, ATCCTCAAggAgAAgCTgggCAgCCTgAgCTTTgCCgATgTgAAggC. DNA sequencing of the mutated *imiS* genes using T7for (TAATACgACTCACTATAgg) and T7rev (CgATCAATAACGAgTCgCC) as the primers was used to confirm the presence of the

mutation and that no other unintended mutations were present in the genes. These DNA sequences were analyzed on the Perkin Elmer ABI 3100 Genetic Analyzer.

To test for the over-expression of mutants, the mutant plasmids were transformed into *E. coli* BL21(DE3) cells, and small-scale cell cultures were used (32). Large-scale 4L preparations were performed using the protocol described above for wild-type ImiS. Zn(II)-loaded samples of ImiS and ImiS mutants were made 100 M in Zn(II) and incubated for 30 minutes on ice. The samples were then dialyzed versus 3 × 1L of metal-free, 50 mM Tris, pH 7.0, at 4 °C over a 6 hour time period in order to remove any unbound Zn(II). These Zn(II)-loaded samples of ImiS and ImiS mutants were diluted to a final enzyme concentration of 5–10 μM. The metal content of these samples was determined using a Varian Liberty 2 Inductively Coupled Plasma Spectrometer with atomic emission spectroscopy detection (ICP-AES). The final dialysis buffer was used as a blank. Calibration curves for all metals tested were based on at least three concentration replicates, and all calibration curves had correlation coefficients of 0.9950 or better. Emission lines were monitored at 213.856, 238.892, 324.754, 259.940, 257.610, and 231.604 nm, the most intense emissions for zinc, cobalt, copper, iron, manganese, and nickel, respectively. Errors in metal content were reported as standard deviations (σ_{n-1}) of replicate samples.

Zn(II)-loaded ImiS and ImiS mutants were dialyzed versus 3 × 2 L of 5 mM phosphate, pH 7.0, over 6 hours. The samples were then diluted with the same buffer to a final concentration of approximately 75 μg/mL. CD spectra were obtained on a JASCO J-810 CD spectropolarimeter, operating at 25 °C. CD spectra were analyzed for secondary structural content using the CONTIN simulation program at DICHROWEB (http://www.cryst.bbk.ac.uk/cdweb/html/home.html) (33,34).

Zn(II)-loaded ImiS and ImiS mutants were diluted with metal-free, 50 mM Tris, pH 7.0, to a final concentration of 2 μM. Fluorescence spectra were obtained at 25 °C using an excitation wavelength of 295 nm on a Perkin Elmer LS55 luminescence spectrophotometer.

Stopped–flow kinetic studies

Hydrolysis of imipenem (10 – 350 μM) by ImiS (120 μM) in 50 mM Tris buffer, pH 7.0, at 2 °C, was followed by electronic absorption at 300 nm and by 280 nm-excited fluorescence emission at > 320 nm (320 nm cutoff filter) on an Applied Photophysics SX18MV spectrophotometer. Time-dependent electronic absorption spectra of Co(II)-substituted ImiS (500 μM) were collected using a photodiode array (PD.1, Applied Photophysics) upon recation with 500 μM imipenem at 2 °C. Kinetic data were fitted to either single or double exponential equations using KinTekSim v. 3.20 software (http://www.kintek-corp.com/). Stopped-flow fluorescence data were also globally-fitted using Applied Photophysics PC ProK Global Analysis software.

Kinetic simulations

Kinetic simulations were conducted using KINSIM (35). The values for flux and integral tolerances were left as the default values of 0.02 and 1×10^{-6}, respectively.

Rapid freeze quench (RFQ) EPR spectra

Samples for RFQ-EPR studies were generated using a modified Update Instruments (Madison, WI) rapid freeze quench (RFQ) system (21). The RFQ system was calibrated by comparing the development of a low-spin Fe(III) EPR signal and the disappearance of a high-spin Fe(III) EPR signal with the associated optical changes at 636 nm using stopped-flow spectrophotometry, upon mixing myoglobin with an excess of sodium azide. The shortest, total effective reaction time that could be achieved with the RFQ system was 10 ms. The initial

concentrations of Co(II)-substituted ImiS and imipemen were 1 mM and 5 mM, respectively. EPR spectra were recorded using a Bruker EleXsys E500 EPR spectrometer equipped with an Oxford Instruments ITC4 temperature controller and an ESR-900 helium flow cryostat. Spectra were recorded at 12 K with 1 mW microwave power. A Bruker ER-4116DM cavity was used, with a resonant frequency of 9.63 GHz (in perpendicular mode), and 10 G (1 mT) field modulation at 100 kHz was employed. Computer simulations of EPR spectra were carried out using the matrix diagonalization program XSophe [Bruker Biopsin GmbH] (36), assuming a spin Hamiltonian $H = \beta\mathbf{gBS} + \mathbf{SDS} + \mathbf{SAI}$, where $S = 3/2$ and $D > 0$ corresponds to an $M_s = |\pm ½\rangle$ ground state Kramers' doublet. For Co(II), generally $D \gg \beta gBS$, and the spectrum is therefore insensitive to the precise value of D (37); in this work the arbitrary value $D = 50$ cm^{-1} was used. The **g** tensor was assumed to have at least axial symmetry as this allows for a unique solution to the spin Hamiltonian in terms of the real g-values, g_z and g_{xy} (or $g_{||}$ and $g^{\perp}$), and the rhombic distortion of the axial zero field splitting, E/D (37). The relationship between the resonance positions, $g_{eff(x,y,z)}$, and these parameters are described in detail elsewhere (38,39). Line widths were simulated using a single strain parameter for each of the principal orientations. Where simulations of spectra are shown that contain more than one species, spectra that could be well- simulated assuming a single set of spin Hamiltonian parameters were used as basis spectra, and linear combinations of two (and no more than two) basis spectra were used to model the spectra collected after reaction times intermediate between those after which the basis spectra were recorded. Contributions of the individual species are estimated as ± 5% of the total spins.

Results

Substrate inhibition

Many enzymes conform to Michaelis-Menten kinetics over a limited range of substrate concentrations but deviate at higher substrate concentrations (40). Steady-state kinetic studies with ImiS and using imipenem or meropenem resulted in Michaelis-Menten plots that indicate significant substrate inhibition (Figure 1). Several substrate inhibition models (competitive, noncompetitive, etc. (26)) were tested to fit the observed steady state kinetic data, and a model defined by uncompetitive substrate inhibition was the model that best fitted the data (line in Figure 1).

Product inhibition studies

The recent crystal structure of CphA showed a unique bicyclic "intermediate" in the active site of the enzyme that is formed by the attack of the invariant hydroxyl group of the 6′-substituent of biapenem (and other carbapenems) on the 3′-carbon of the five-membered ring (11). Garau *et al*. argued that the formation of the second ring in the product occurs after C-N bond cleavage (11). To ascertain whether this bicyclic, hydrolyzed carbapenem is catalytically-competent, we hydrolyzed imipenem with ImiS and with L1. L1 and ImiS were removed from the solutions by ultrafiltration, and the products were analyzed with ^{1}H NMR spectroscopy and LC-MS (see Supplementary Materials). There were no differences in the mass spectra or the NMR spectra of the two products. Neither product absorbed in the UV-Vis region about 280 nm.

Therefore, the ImiS- and L1-generated products were used in product inhibition studies. The ImiS-generated product inhibited ImiS with a K_i of 53 ± 5 μM and inhibited L1 with a K_i of 615 ± 50 μM. The L1-generated product inhibited ImiS with a K_i of 4 ± 1 mM and inhibited L1 with a K_i of 2 ± 1 mM. Clearly, the ImiS-generated product is distinct from the L1-generated product.

pH Dependence studies

pH Dependence kinetic studies can be used to probe for groups with ionizable protons associated on the free enzyme, free substrate, or the enzyme-substrate complex (40). In pH dependence studies on Zn(II)-containing ImiS, a relatively narrow pH range of 5.0 to 8.5 was used because ImiS precipitated at pH values below 5.0 and above 8.5. A multicomponent buffer, MTEN (28), was used to minimize buffer and ionic strength effects. The log k_{cat} and log (k_{cat}/K_M) versus pH plots (Figure 2) for hydrolysis of imipenem by Zn(II)-containing ImiS were fitted with Leonara (29); however, no pK_a values above 5.5 or below 8.0 were revealed. Similar results have been reported for the dinuclear Zn(II)-containing β-lactamases L1 and CcrA (18,41). pH Dependence plots for Co(II)-substituted ImiS with imipenem also did not reveal any inflection points (data not shown).

Solvent isotope studies

Solvent isotope studies have been extensively used in the literature to probe reaction mechanisms of enzymes, specifically to identify any rate-limiting proton transfers (31). The hydrolysis of imipenem by ImiS yielded a solvent isotope effect (k^H/k^D) of 1.7 ± 0.2, suggesting a proton transfer during a nucleophilic reaction. A proton inventory of ImiS yielded a k_{cat} versus mole fraction of D_2O that was best fitted to a multiple proton in flight model (Figure 3); however, we cannot unambiguously rule out the one or two proton in flight models (30). Similar proton inventories have been reported for dinuclear Zn(II)-containing L1 and CcrA (28,41).

K224T and N233S Mutants of ImiS

A lysine is located at position 224 in all sequenced MβL's except in L1 from *S. maltophila* (6). Lys224 has been proposed to be involved in substrate binding via electrostatic interactions with the invariant carboxylate group of the β-lactam-containing antibiotics (11,42,43). To test this hypothesis Lys224 was mutated to a threonine using site-directed mutagenesis. Bordo and Argos have reported that threonine is the "safest" substitution in mutagenesis studies for exposed lysines (44). Small-scale cultures were used to show that the K224T mutant could be over-expressed and purified at levels comparable to wild-type ImiS. CD and fluorescence spectra of the K224T mutant were similar to those of wild-type ImiS (data not shown), suggesting that the point mutation does not result in large structural changes in the enzyme.

Metal analyses on as-isolated and Zn(II)-loaded K224T demonstrated that the mutant binds 0.80 and 0.78 equivalents of Zn(II), respectively, which is similar to the metal content of wild-type ImiS (Table 1). Steady-state kinetics revealed that this mutant exhibited a 16-fold drop in k_{cat} and 4-fold increase in K_M when using imipenem as a substrate (Table 1). In studies using meropenem as substrate, the K224T mutant exhibited no change in K_M and a 740-fold decrease in k_{cat} (Table 1).

An asparagine is located at position 233 in all MβL's except L1 from *S. maltophila* (subclass B3) (45), BlaB (subclass B1) (46), and IND-1 from *Chryseobacterium* species (subclass B1) (47). The N233S mutant could be over-expressed and purified at levels comparable to that of wild-type ImiS. This mutant also exhibited CD and fluorescence spectra similar to those of wild-type ImiS (25), suggesting that the point mutation did not cause a change in the structure of the enzyme. Metal analyses revealed that as-isolated and Zn(II)-loaded N233S bound 0.77 and 0.99 equivalents of Zn(II), respectively (Table 1). Steady-state kinetics revealed that the N233S mutant exhibited steady-state kinetic constants similar to those of wild-type ImiS (Table 1).

Stopped-flow kinetic studies

In initial stopped-flow UV-Vis studies, we reacted Co(II)-substituted ImiS with imipenem, and we monitored the reaction using diode array detection, particularly in the 500–650 nm region of the spectra, in an effort to probe the ligand field transitions of high-spin Co(II) during the course of the reaction. In all of the experiments that we conducted, there were no observable changes in the intensities of the ligand field bands. Therefore, we chose to monitor the change in absorbance of the substrate during the course of the reaction. The rate of imipenem hydrolysis, monitored by stopped-flow spectrophotometry (Figure 4), was a complex function of the concentration of imipenem and exhibited uncompetitive substrate inhibition (Figure 1). A single exponential fit to the single turnover progress curve with 100 μM imipenem returned a turnover rate of 97 s^{-1} at 2 °C.

Single turnover (100 μM imipenem/meropenem and 120 μM ImiS) reactions were also probed with stopped-flow fluorescence studies, which monitor tryptophan fluorescence of the enzyme during catalysis. The resulting stopped-flow fluorescence time courses were biphasic and showed a substantial quenching of fluorescence over the first 10 milliseconds of the reaction, followed by a relatively slow regain to baseline levels over the subsequent 45 milliseconds of the reaction. The stopped-flow fluorescence data were fitted with a double exponential equation, which yielded a rate of 160 ± 4 s^{-1} for the initial quenching phase and a rate of 98 ± 1 s^{-1} for the slower fluorescence regain phase (Figure 5). Additional experiments were conducted at higher substrate and lower ImiS concentrations. However as with the stopped-flow UV-Vis studies, the rates of fluorescence quench and regain were lower at substrate concentrations > 200 μM.

Global fittings and KINSIM simulations

By using previously reported kinetic mechanisms (17,40,48) and PC ProK global fitting software, the stopped-flow fluorescence data were fitted. The simple Michaelis-Menten mechanism was tested first, and more complicated mechanisms were subsequently tested. The simplest mechanism that sufficiently fitted the data is shown in Scheme 1; this mechanism was previously proposed for dinuclear Zn(II)-containing M L L1 from *S. maltophilia* when reacted with meropenem or cefaclor (48) (Table 2). By using the rate constants (Table 2), the mechanism in Scheme 1, and KINSIM (35), we could suitably simulate the stopped-flow fluorescence and UV-Vis data (lines in Figures 4 and 5). The global fittings and kinetic simulations show that the rate constants determined with single turnover experimentsare equal to k_5 and k_7. This scenario supports our analyses that the second and third steps (k_4 and k_6, Scheme I) of the mechanism are essentially irreversible.

The values obtained from the global fittings (Table 2) were used to calculate steady-state parameters according to $k_{cat} = (k_3)(k_5)(k_7)/(k_5)(k_7)+(k_3)(k_7)+(k_3)(k_5)$ and $K_M = k_{cat} \times \{(k_2+k_3)/(k_1)(k_3)\}$. The theoretical steady-state kinetic constants are k_{cat} = 58 s^{-1} and K_M = 39 μM. The theoretical values of k_{cat} and K_M are within a factor of 3 of the experimentally-determined values at 2 °C: k_{cat} = 130 ± 30 s^{-1} and K_M = 90 ± 50 μM.

Rapid freeze quench EPR studies

The EPR spectrum of Co(II)-substituted ImiS is shown in Figure 6A and was simulated assuming a single paramagnetic species with $S = 3/2$, $M_S = |\pm 1/2\rangle$, $g_{x,y} = 2.25$, $g_z = 2.31$, $E/D = 0.076$ (Figure 4B). No other Co(II) species were detected between 4 K and 13 K and at microwave powers up to 40 mW – an $M_S = |\pm 3/2\rangle$ signal that was evident in some preparations of ImiS upon addition of substoichiometric Co(II) (12), was not observed in the present work; this may be related to the higher pH employed (7.0 *vs.* 6.5) and the known propensity of Co (II) to adopt higher coordination numbers when possible (49). Upon reaction of ImiS with imipenem for 10 ms, the spectrum (Figure 6C) had clearly changed, and subtraction of the

resting signal indicated the appearance of a rhombic signal (Figure 7A) for which only the two low field resonances could be resolved. From the EPR spectrum after 21 ms reaction time (Figure 6D), a second species (Figure 7B) could be clearly isolated by subtraction of the resting signal and was simulated (Figure 7C) using $S = 3/2$, $M_S = |\pm 1/2\rangle$, $g_{x,y} = 2.24$, $g_z = 2.18$, $E/D = 0.145$, $A_y(^{59}Co) = 40$ G. It should be noted that while the lineshape was best-simulated including an unresolved hyperfine coupling on the lowest field feature (g_y for $M_S = |\pm 1/2\rangle$ of $S = 3/2$), the experimental data only suggested three barely-resolved hyperfine lines, and the data were not of sufficient signal-to-noise to confirm a full hyperfine pattern by the use of higher derivatives. The '21 ms' experimental spectrum (Figure 6D) was well-modeled by the addition of the simulations of the resting signal, accounting for 94% of the spins, and the rhombic signal, accounting for 6%. It is not clear whether the rhombic signal after 10 ms is the same as that after 21 ms; while the two lower field resonances clearly coincide, the high field g_z resonance may be either broadened or shifted in the '10 ms' spectrum compared to the '21 ms' spectrum, perhaps indicating some very subtle structural differences. The EPR spectrum continued to change upon further reaction. The spectrum after 32 ms (Figure 6F) was again composed of the resting and rhombic signals (Figures 6G and 7D), and after 73 ms (Figure 6E) the intensity of the rhombic signal was greater than that after 21 ms by a factor of about 1.6, corresponding to 10% of the total Co(II). When rapid-freeze-quenched samples were thawed and refrozen after 2 s, an EPR signal (Figure 6I) consisting of 35% resting signal and 65% of a third distinct signal, the 'product' signal, was observed. The product signal was isolated (Figure 7F) by subtraction of the resting signal from Figure 6I and could be simulated (Figure 7G) assuming $S = 3/2$, $M_S = |\pm 1/2\rangle$, $g_{x,y} = 2.35$, $g_z = 2.12$, $E/D = 0.13$. An enzyme bound product signal was also observed in RFQ EPR spectra of B3 metallo-β-lactamase L1 (21).

Discussion

There have been many reports on the reaction mechanisms of dinuclear Zn(II)-containing M L's (from subgroups B1 and B3). In studies using CcrA and L1 and nitrocefin as substrate, a ring-opened, nitrogen anionic intermediate was identified, and kinetic studies revealed that the protonation of this intermediate was rate-limiting (17–20,41). RFQ-EPR studies demonstrated that this intermediate yielded a novel EPR signal (21). A similar intermediate has not been observed in studies with *B. cereus* β-lactamase II (50). Spencer and coworkers later extended mechanistic studies on L1 using other substrates such as cefaclor and meropenem (48). Kinetic analyses revealed that β-lactam bond cleavage is rate-limiting with these substrates, and these authors hypothesized that the intermediate observed when nitrocefin is used as a substrate is unique to nitrocefin and due to the highly-conjugated, *bis*-nitro-substituted styryl substituent (48). Therefore, the reaction mechanisms of the B1 and B3 MβL's are becoming clearer. In contrast, there is little mechanistic information (except that inferred by a recent crystal structure on CphA (11) and that proposed based on very recent computational studies on CphA (51, 52)) on any of the mononuclear Zn(II)-containing B2 MβL's.

Many enzymes, including L1 (27), exhibit substrate inhibition at high substrate concentrations (29); however, the concentrations of substrate required to inhibit ImiS are relatively low (>200 μM). Analysis of the steady-state kinetic data demonstrate that the observed substrate inhibition in ImiS is uncompetitive (Figure 1), which indicates that the inhibitory substrate molecule binds to the ES (or species derived from ES) complex. With ImiS, it is possible that the substrate could bind with the β-lactam carbonyl or the β-lactam nitrogen coordinated to the metal ion, with one binding mode being the catalytically active mode and one mode describing an inhibited enzyme. The scenario would be expected to result in competitive substrate inhibition. It has been proposed for the B1 and B3 MβL's that there is a loop that extends over the active site and that may play a role in catalysis by "clamping down" and activating substrate during catalysis (42,53,54). In the case of CphA (and presumably ImiS, there is an α-helix (α3) that is located where this loop is in other enzymes (11). It is possible that a second molecule of

substrate could bind to ES and prevent this α-helix from "clamping down" on substrate. Further studies are required to better understand substrate inhibition in ImiS.

Our first efforts to probe mechanism used pH dependence and solvent isotope studies. As previously reported for L1 and CcrA (18,28,41), there are no apparent inflection points in the pH dependence plots. With L1 and CcrA, it was argued that the pK_a of the bridging solvent group was much lower than 5, as a result of bridging two divalent Zn(II) ions. Based on extensive literature precedents on Zn(II) hydrolases (55–60), it is possible that the Zn(II) in ImiS in conjunction with Asp120 could generate a hydroxide that has a $pK_a < 5$. However, recent computational studies (52), along with predictions from the crystallographic studies (11), suggest that the nucleophile in CphA is not generated by Zn(II) and that the nucleophile is generated by assistance of His118 and Asp120 (11) or solely by Asp120 (52). In addition, our RFQ-EPR studies suggest that there are only 5 ligands bound to the metal during catalysis, and these ligands are most likely three amino acid residues (Asp120, Cys221, and His263) and 2 points of attachment from the substrate (see below) (11). If in fact the reactive nucleophile is generated without the direct coordination to the metal ion, we hypothesize that both Asp120 and His118 participate in the generation of this nucleophile and that the pK_a of this solvent molecule is atypically low.

ImiS exhibited a solvent isotope effect that was very similar to that of dinuclear Zn(II)-containing L1 and CcrA (28,41), however, it is possible that there are > 1 rate-significant protons in flight for ImiS. These data demonstrate that there is a rate-significant proton transfer in the reaction catalyzed by ImiS (30). Given that the rate-limiting step is most likely C-N bond cleavage (see below), one potentially important proton transfer could be to the ring nitrogen in product. It is also possible that a proton transfer from the solvent molecule to generate the putative nucleophile could explain why multiple, rate-limiting proton transfers are possible with ImiS.

The roles of Lys224 and Asn233 were probed using site directed mutagenesis. Several groups have demonstrated that Lys224 is involved in substrate binding to several of the dinuclear-Zn (II)-containing MβL's (28,42,43,61–64). In fact, the recent structure of CphA bound to product suggests that Lys224 interacts with the 3′-carboxylate on substrate (11), and computational studies support a role of Lys224 in substrate binding (51). In contrast, our studies on the K224T mutant indicate that Lys224 is involved with catalysis, suggesting that the orientation of the 3′ carboxylate is catalytically important. Crystallographic and computational studies suggested a role of the backbone amide of Asn233 forming a hydrogen bond with the 3′ carboxylate on substrate (11,51), and computational studies additionally suggested that the side-chain amide of Asn233 hydrogen bonds with the β-lactam carbonyl on substrate (52). Our mutagenesis studies demonstrate that the side chain of Asn233 is not involved substrate binding or catalysis, which supports the former prediction but not the latter.

Stopped-flow fluorescence and UV-Vis studies were used next to probe the mechanism of ImiS. SF-fluorescence traces were similar in appearance to those of L1 (32,48). The fluorescence properties of L1 are due to a single Trp (Trp37), which is located in close proximity to the dinuclear Zn(II) site (22). It is likely that the fluorescence changes upon substrate binding to ImiS are also due to a single tryptophan, possibly Trp87, which lies near the putative substrate binding site and within 10 Å of Zn(II) in CphA (11). SF-fluorescence studies of 120 μM ImiS with 100 μM imipenem (or meropenem) resulted in a rapid decrease in fluorescence ($k_{obs} = 160\ s^{-1}$) and relatively slow regain in fluorescence ($k_{obs} = 98\ s^{-1}$). SF-UV-Vis studies, which monitored the hydrolysis of the β-lactam bond in substrate (48), showed a rapid decrease in absorbance that was best fitted with a single exponential equation yielding a $k_{obs} = 97\ s^{-1}$. As previously suggested for L1 (48), the regain of fluorescence due to substrate

loss and the loss of absorbance are due to β-lactam hydrolysis in ImiS, and this step is probably the rate determining step.

In an effort to offer a minimal kinetic mechanism that describes the data, global analyses and KINSIM were used to test several different kinetic mechanisms. The single turnover data of ImiS were best fitted/simulated using the kinetic mechanism and rate constants shown in Scheme 1 and Table 2, respectively. The minimal kinetic mechanism of ImiS shown in Scheme 1 is very similar to that of L1 (48) and suggests that the rate-limiting step is β-lactam hydrolysis. This mechanism also suggests the existence of second ES complex (ES* in Scheme 1). Absence of ES* in our global analyses and KINSIM fits resulted in poor fits of the data.

EPR spectroscopy of ImiS upon reaction with imipenem identified two new imipenem-dependent signals due to isolated Co(II). One, the rhombic signal, is indicative of a highly-distorted geometry and suggestive of five-fold coordination of Co(II). The partial resolution of ^{59}Co hyperfine coupling of 40 G (4.3×10^{-3} cm^{-1}) indicates a narrow intrinsic EPR line and is entirely consistent with such a structure, in which the rigid ligand environment necessary to constrain the distorted structure precludes large strains in **g** and/or the zero-field splitting parameters. From a structural basis, therefore, it is likely that the rhombic signal corresponds to either ES* or EI in the reaction proposed in Figure 8. In principle, the kinetic studies should provide further information as to which intermediate likely accumulates in sufficient amounts to be observed by EPR. In the case of ImiS, however, the situation is complicated by the substrate inhibition observed with imipenem. In the EPR experiment, the initial substrate concentration in the reaction mixture (after mixing) was 2.5 mM, and by extrapolation of Figure 1, the overall reaction rate may be expected to be of the order of 10% of that of the optimum rate. Uncompetitive inhibition, which best fits the data for ImiS and imipenem (Figure 1), implies further binding of imipenem to either ES, ES*, or EI, rather than a second, nonproductive mode of binding to the hitherto uncomplexed enzyme. Because the inhibition is not competitive, any molecule of imipenem to interact with the active site of ImiS will rapidly form ES and the imipenem pool will be initially depleted according to k_1 and k_2, and more slowly as fewer naked ImiS molecules are available. As the enzyme and substrate are mixed in a 1:1 ratio, and as k_1 is high and $K_i > K_m$, substrate inhibition will only be a factor during the mixing time, when local relative concentrations of imipenem may be higher than the eqiulibrium concentration. The mixing time is estimated to be ~ 1 ms. This is comparable with the optimum rate of formation of ES*, and thus, the rate of formation of ES* from ES is unlikely to be impeded by more than a factor of two or so if this is indeed the step inhibited by excess substrate. Thus, ES* formation is likely to be complete between 1 and 2 ms after mixing. Formation of EI is expected after a further 7 ms, *i.e.*, after 8 – 9 ms, and the rhombic species observed after 10 ms is, therefore, assignable to the EI complex. While the simplest interpretation of the EPR spectra beyond 10 ms invoked a single species (the rhombic) in addition to the resting species, the kinetics suggest an alternative explanation, that g_z of the rhombic species is indeed unresolved, as in the signal isolated by difference from the 10 ms-reacted sample, and that the appearance of a resolved high field feature in spectra recorded at longer reaction times is due to a contribution from the product species. While the EPR data are not of sufficient quality to differentiate these two explanations, the latter is entirely consistent with the kinetics, as the product complex would be expected to begin accumulating at around 18 – 19 ms. Thus it is proposed that the rhombic species represents EI and the product species represents EP.

These data and previous crystallographic data (11) allow for us to propose a reaction mechanism for ImiS (Figure 8). In the first step, substrate binds to the active site replacing a water molecule. Initially, the carboxylate on substrate interacts with Lys224 and Zn(II); however based on kinetic simulations, we believe that a second ES complex (labelled ES*) forms. We postulate that the Zn(II)-substrate nitrogen interaction forms in ES*, generating a

5-coordinate metal center. In our proposed mechanism, the nucleophile is generated by Asp120 and His118 as previously proposed (11); this nucleophile attacks the β-lactam carbonyl, possibly activated by His196 (11), to generate a tetrahedral intermediate, which we have labeled EI. It is important to note that the recent computational study suggested that a tetrahedral intermediate does not form in the proposed mechanism of CphA (52), and our data cannot support nor refute this hypothesis. It is entirely possible that EI is in fact a ring-opened, unprotonated species, similar to that reported in studies with CcrA and L1 when reacted with nitrocefin (17,19,21). In either case, a proton must be transferred to the ring-opened, nitrogen to generate product. We have also included the structure of the enzyme-product complex in the mechanism because this species was detected by RFQ-EPR studies. The inclusion of an EP complex in our kinetic simulations did not affect the fits as long as the rate of formation of EP is much faster than the breakdown of EI. Our spectroscopic data do not support the previous hypothesis (52) of Asp120 releasing from the metal ion during catalysis, yielding a 4-coordinate intermediate.

The recent crystal structure of CphA showed the presence of a bicyclic product of biapenem in the active site of the enzyme (11). The authors proposed that after β-lactam bond cleavage, a substantial bond rotation occurs that allows for the proton on the hydroxyethyl substituent found on all carbapenems to transfer to the 2′-position on the five-membered ring of substrate and for the nucleophilic attack of the oxygen at the 3′-position. Due to steric constraints, it is clear that this cyclization occurs after C-N bond cleavage. Our product inhibition data strongly suggest that the bicyclic product is kinetically-competent and is the final product of the reaction catalyzed by ImiS.

The results described herein demonstrate that MβL's from each of the distinct subclasses share a common rate-determining step, which is C-N bond cleavage. This fact suggests that inhibitors designed on this step will inhibit all MβL's, regardless of whether the enzymes are mono- or dinuclear Zn(II)-containing enzymes.

Acknowledgements

The authors would like to thank Professor Hua Guo of the University of New Mexico for helpful discussions, particularly those involving the timing of the formation of the bicyclic product.

Abbreviations

CD
: circular dichroism

EPR
: electron paramagnetic resonance

IPTG
: isopropyl-β-*D*-thiogalactopyranoside

LB
: Luria-Bertani

LC-MS
: liquid chromatography-mass spectrometry

MβL
: metallo-β-lactamase

PAGE

polyacrylamide gel electrophoresis

RFQ

rapid freeze quench

SDS

sodium dodecyl sulfate

Tris

tris(hydroxymethyl)aminomethane

References

1. Walsh CT, Wright GD. Introduction: Antibiotic resistance. Chem Rev 2005;105:391–393. [PubMed: 15700949]
2. Neu HC. The crisis in antibiotic resistance. Science 1992;257:1064–73. [PubMed: 1509257]
3. Heinz U, Adolph HW. Metallo-β-lactamases: two binding sites for one catalytic metal ion? CMLS, Cell Mol Life Sci 2004;61:2827–2839.
4. Walsh TR, Toleman MA, Poirel L, Nordmann P. Metallo-β-lactamases: the quiet before the storm? Clin Microbiol Rev 2005;18:306–325. [PubMed: 15831827]
5. Galleni M, Lamotte-Brasseur J, Rossolini GM, Spencer J, Dideberg O, Frere JM. Standard numbering scheme for class B β-lactamases. Antimicro Agents Chemo 2001;45:660–663.
6. Garau G, Garcia-Saez I, Bebrone C, Anne C, Mercuri P, Galleni M, Frere JM, Dideberg O. Update of the standard numbering scheme for class B β-lactamases. Antimicro Agents Chemo 2004;48:2347–2349.
7. Valladares MH, Felici A, Weber G, Adolph HW, Zeppezauer M, Rossolini GM, Amicosante G, Frere JM, Galleni M. Zn(II) dependence of the *Aeromonas hydrophila* AE036 Metallo-β-Lactamase Activity and Stability. Biochemistry 1997;36:11534–11541. [PubMed: 9298974]
8. Janda JM, Duffey PS. Mesophilic Aeromonads in human diseases: current taxonomy, laboratory identification, and infectious disease spectrum. Rev Infect Dis 1988;10:980–987. [PubMed: 3055195]
9. Jones BL, Wilcox MH. *Aeromonas* infections and their treatment. J Antimicrob Chemo 1995;35:453–461.
10. Borrell N, Figueras M, Guarro J. Phenotypic identification of *Aeromonas* genomospecies from clinical and environmental sources. Can J Microbiol 1998;44:103–108. [PubMed: 9575026]
11. Garau G, Bebrone C, Anne C, Galleni M, Frere JM, Dideberg O. A metallo-β-lactamase enzyme in action: crystal structure of the monozinc carbapenemase CphA and its complex with biapenem. J Mol Biol 2005;345:785–795. [PubMed: 15588826]
12. Crawford PA, Yang KW, Sharma N, Bennett B, Crowder MW. Spectroscopic studies on cobalt(II)-substituted metallo-β-lactamase ImiS from *Aeromonas veronii bv. sobria*. Biochemistry 2005;44:5168–5176. [PubMed: 15794654]
13. Toney JH, Moloughney JG. Metallo-β-lactamase inhibitors: promise for the future? Curr Opin Invest Drugs 2004;5:823–826.
14. Siemann S, Clarke AJ, Viswanatha T, Dmitrienko GI. Thiols as classical and slow-binding inhibitors of IMP-1 and other binuclear metallo-β-lactamases. Biochemistry 2003;42:1673–1683. [PubMed: 12578382]
15. Heinz U, Bauer R, Wommer S, Meyer-Klaucke W, Papamichaels C, Bateson J, Adolph HW. Coordination geometries of metal ions in *D*- or *L*-captopril-inhibited metallo-β-lactamases. J Biol Chem 2003;278:20659–20666. [PubMed: 12668674]
16. Buynak JD, Chen H, Vogeti L, Gadhachanda VR, Buchanan CA, Palzkill T, Shaw RW, Spencer J, Walsh TR. Penicillin-derived inhibitors that simultaneously target both metallo- and serine-β-lactamases. Bioorg Med Chem Lett 2004;14:1299–1304. [PubMed: 14980686]
17. McManus-Munoz S, Crowder MW. Kinetic mechanism of metallo-β-lactamase L1 from *Stenotrophomonas maltophilia*. Biochemistry 1999;38:1547–1553. [PubMed: 9931021]

18. Wang Z, Benkovic SJ. Purification, characterization, and kinetic studies of soluble *Bacteroides fragilis* Metallo-β-Lactamase. J Biol Chem 1998;273:22402–22408. [PubMed: 9712862]
19. Wang Z, Fast W, Benkovic SJ. Direct observation of an enzyme-bound intermediate in the catalytic cycle of the metallo-β-lactamase from *Bacteroides fragilis*. J Am Chem Soc 1998;120:10788.
20. Wang Z, Fast W, Benkovic SJ. On the mechanism of the metallo-β-lactamase from *Bacteroides fragilis*. Biochemistry 1999;38:10013–10023. [PubMed: 10433708]
21. Garrity JD, Bennett B, Crowder MW. Direct evidence that reaction intermediate in metallo-β-lactamase is metal bound. Biochemistry 2005;44:1078–1087. [PubMed: 15654764]
22. Garrity JD, Pauff JM, Crowder MW. Probing the dynamics of a mobile loop above the active site of L1, a metallo-β-lactamase from *Stenotrophomonas maltophilia*, via site-directed mutagenesis and stopped-flow fluorescence spectroscopy. J Biol Chem 2004;279:39663–39670. [PubMed: 15271998]
23. Bounaga S, Laws AP, Galleni M, Page MI. The mechanism of catalysis and the inhibition of the *Bacillus cereus* zinc-dependent β-lactamase. Biochem J 1998;331:703–711. [PubMed: 9560295]
24. Dal Peraro M, Llarrull LI, Rothlisberger U, Vila AJ, Carloni P. Water-assisted reaction mechanism of monozinc β-lactamases. J Am Chem Soc 2004;126:12661–12668. [PubMed: 15453800]
25. Crawford PA, Sharma N, Chandrasekar S, Sigdel T, Walsh TR, Spencer J, Crowder MW. Over-expression, purification, and characterization of metallo-β-lactamase ImiS from *Aeromonas veronii bv. sobria*. Prot Express Purif 2004;36:272–279.
26. Webb, JL. Enzyme and Metabolic Inhibitors. 1. Academic Press; New York: 1963.
27. Crowder MW, Walsh TR, Banovic L, Pettit M, Spencer J. Overexpression, purification, and characterization of the cloned metallo-β-lactamase L1 from *Stenotrophomonas maltophilia*. Antimicro Agents Chemo 1998;42:921–926.
28. Yanchak MP, Taylor RA, Crowder MW. Mutational analysis of metallo-β-lactamase CcrA from *Bacteroides fragilis*. Biochemistry 2000;39:11330–11339. [PubMed: 10985778]
29. Cornish-Bowden, A. Analysis of Enzyme Kinetic Data. Oxford University Press; Oxford: 1995.
30. Venkatasubban KS, Schowen RL. The proton inventory technique. CRC Crit Rev Biochem 1984;17:1–44. [PubMed: 6094099]
31. Schowen, KBJ. Transition States of Biochemical Processes. Gandour, RD.; Schowen, RL., editors. Plenum Press; New York: 1978. p. 225-283.
32. Carenbauer AL, Garrity JA, Periyannan G, Yates RB, Crowder MW. Probing substrate binding to metallo-β-lactamase L1 from *Stenotrophomonas maltophilia* by using site-directed mutagenesis. BMC Biochemistry 2002;3:4–10. [PubMed: 11876827]
33. Lobley A, Wallace BA. Dichroweb: A website for the analysis of protein secondary structure from circular dichroism spectra. Biophys J 2001;80:1570.
34. Lobley A, Whitmore L, Wallace BA. DICHROWEB: an interactive website for the analysis of protein secondary structure from circular dichroism spectra. Bioinformatics 2002;18:211–212. [PubMed: 11836237]
35. Frieden C. Numerical integration of rate equations by computer. Trends Biochem Sci 1993;18:58–60. [PubMed: 8488560]
36. Hanson, GR.; Gates, KE.; Noble, CJ.; Mitchell, A.; Benson, S.; Griffin, M.; Burrage, K. EPR of Free Radicals in Solids: Trends in Methods and Applications. Shiotani, M.; Lund, A., editors. Kluwer Press; Dordrecht: 2003. p. 197-237.
37. Bennett B. EPR of Co(II) as a structural and mechanistic probe of metalloprotein active Sites: characterization of an aminopeptidase. Curr Topics Biophys 2002;26:49–57.
38. Bennett B, Holz RC. EPR studies on the mono- and dicobalt(II)-substituted forms of the aminopeptidase from *Aeromonas proteolytica*. Insight into the catalytic mechanism of dinuclear hydrolases. J Am Chem Soc 1997;119:1923–1933.
39. Bennett B, Holz RC. Spectroscopically distinct cobalt(II) sites in heterodimetallic forms of the aminopeptidase from *Aeromonas proteolytica*: Characterization of substrate binding. Biochemistry 1997;36:9837–9846. [PubMed: 9245416]
40. Fersht, A. Enzyme Structure and Mechanism. 2. W. H. Freeman and Co; New York: 1985.

41. Garrity JD, Carenbauer AL, Herron LR, Crowder MW. Metal binding Asp-120 in metallo-β-lactamase L1 from *Stenotrophomonas maltophilia* plays a crucial role in catalysis. J Biol Chem 2004;279:920–927. [PubMed: 14573595]
42. Ullah JH, Walsh TR, Taylor IA, Emery DC, Verma CS, Gamblin SJ, Spencer J. The crystal structure of the L1 metallo-β-lactamase from *Stenotrophomonas maltophilia* at 1.7 angstrom resolution. J Mol Biol 1998;284:125–136. [PubMed: 9811546]
43. Concha NO, Rasmussen BA, Bush K, Herzberg O. Crystal structure of the wide-spectrum binuclear zinc β-lactamase from *Bacteroides fragilis*. Structure 1996;4:823–836. [PubMed: 8805566]
44. Bordo D, Argos P. Suggestions for safe residue substitutions in site-directed mutagenesis. J Mol Biol 1991;217:721–729. [PubMed: 2005621]
45. Walsh TR, Hall L, Assinder SJ, Nichols WW, Cartwright SJ, MacGowan AP, Bennett PM. Sequence analysis of the L1 metallo-β-lactamase from *Xanthomonas maltophilia*. Biochim Biophys Acta 1994;1218:199–201. [PubMed: 8018721]
46. Rossolini GM, Franceschini N, Riccio ML, Mercuri PS, Perilli M, Galleni M, Frere JM, Amicosante G. Characterization and sequence of the *Chryseobacterium (Flavobacterium) meningosepticum* carbapenemase: A new molecular Class B β-lactamase showing a broad substrate profile. Biochem J 1998;332:145–152. [PubMed: 9576862]
47. Bellais S, Poirel L, Leotard S, Naas T, Nordmann P. Genetic diversity of carbapenem-hydrolyzing metallo-β-lactamases from *Chryseobacterium (Flavobacterium) indologenes*. Antimicro Agents Chemo 2000;44:3028–3034.
48. Spencer J, Clark AR, Walsh TR. Novel mechanism of hydrolysis of therapeutic β-Lactams by *Stenotrophomonas maltophilia* L1 metallo-β-lactamase. J Biol Chem 2001;276:33638–33644. [PubMed: 11443136]
49. Kremer-Aach A, Klaui W, Bell R, Strerath A, Wunderlich H, Mootz D. Cobalt as a probe for zinc in metalloenzyme model compounds? A comparison of spectroscopic features and coordination geometry of four- and five-coordinate complexes. Inorg Chem 1997;36:1552–1563. [PubMed: 11669742]
50. Rasia RM, Vila AJ. Mechanistic study of the hydrolysis of nitrocefin mediated by *B. cereus* metallo-β-lactamase. ARKIVOC 2003;3:507–516.
51. Xu D, Zhou Y, Xie D, Guo H. Antibiotic binding to monozinc CphA β-lactamase from *Aeromonas hydrophila*: Quantum mechanical/molecular mechanical and density functional theory studies. J Med Chem 2005;48:6679–6689. [PubMed: 16220984]
52. Xu D, Xie D, Guo H. Catalytic mechanism of class B2 metallo-β-lactamase. J Biol Chem 2006;281:8740–8747. [PubMed: 16423823]
53. Huntley JJA, Fast W, Benkovic SJ, Wright PE, Dyson HJ. Role of a solvent-exposed trytophan in the recognition and binding of antibiotic substrates for a metallo-β-lactamase. Protein Sci 2003;12:1368–1375. [PubMed: 12824483]
54. Scrofani SDB, Chung J, Huntley JJA, Benkovic SJ, Wright PE, Dyson HJ. NMR Characterization of the metallo-β-lactamase from *Bacteroides fragilis* and its interaction with a tight-binding inhibitor: Role of an active-site loop. Biochemistry 1999;38:14507–14514. [PubMed: 10545172]
55. Auld, DS. Metal Sites in Proteins and Models: Phosphatases, Lewis Acids, and Vanadium. Hill, HAO.; Sadler, PJ.; Thomson, AJ., editors. Springer-Verlag; New York: 1997. p. 29-50.
56. Bertini I, Luchinat C, Scozzafava A. The acid base equilibria of carbonic anhydrase. Inorg Chim Acta 1980;46:85–89.
57. Bertini I, Luchinat C. The reaction pathways of zinc enzymes and related biological catalysts. Bioinorg Chem 1994:37–106.
58. Christianson, DW.; Cox, JD. Annu Rev Biochem. 1999. p. 33-57.Ann. Rev.
59. Denisov VP, Jonsson BH, Halle B. Dynamics of functional water in the active site of native carbonic anhydrase from ^{17}O magnetic relaxation dispersion. J Am Chem Soc 1999;121:2327–2328.
60. Vallee BL, Auld DS. Active-site zinc ligands and activated H_2O of zinc enzymes. Proc Nat Acad Sci 1990;87:220–224. [PubMed: 2104979]
61. Toney JH, Wu JK, Overbye KM, Thompson CM, Pompliano DL. High-yield expression, purification, and characterization of active, soluble *Bacteroides fragilis* Metallo-β-Lactamase, CcrA. Prot Express Purif 1997;9:355–362.

62. Spencer J, Read J, Sessions RB, Howell S, Blackburn GM, Gamblin SJ. Antibiotic recognition by binuclear metallo-β-lactamases revealed by X-ray crystallography. J Am Chem Soc 2005;127:14439–14444. [PubMed: 16218639]

63. Park H, Brothers EN, Merz KM. Hybrid QM/MM and DFT investigations of the catalytic mechanism and inhibition of the dinuclear zinc metallo-β-lactamase CcrA from *Bacteroides fragilis*. J Am Chem Soc 2005;127:4232–4241. [PubMed: 15783205]

64. Suarez D, Brothers EN, Merz KM. Insights into the structure and dynamics of the dinuclear zinc beta-lactamase site from *Bacteroides fragilis*. Biochemistry 2002;41:6615–6630. [PubMed: 12022865]

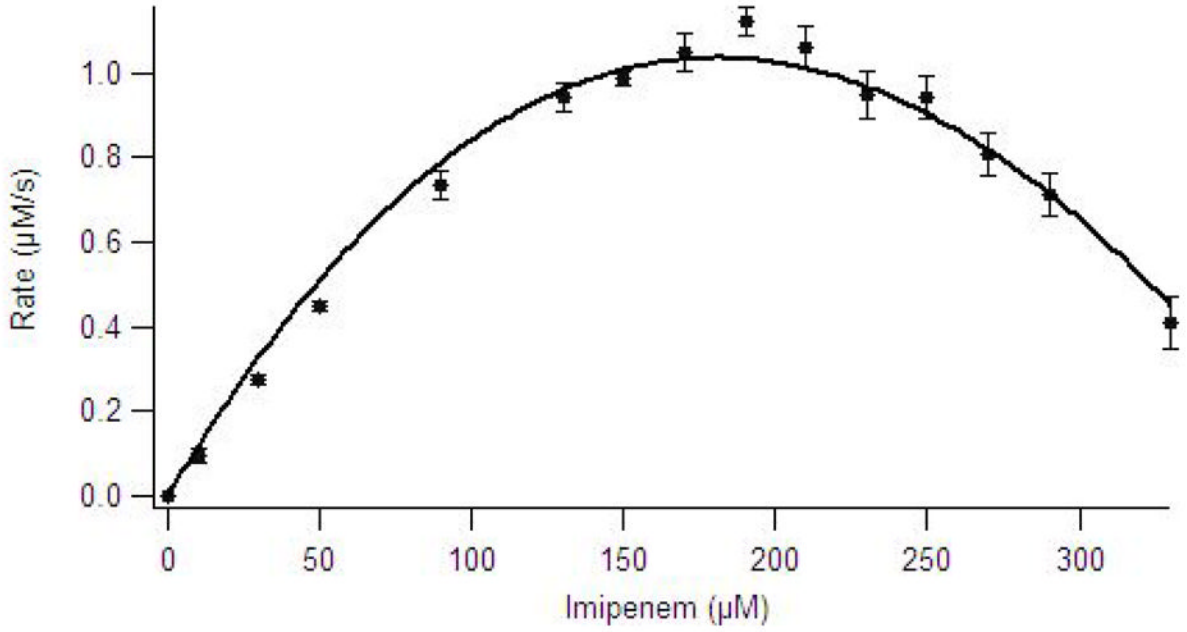

Figure 1.
Michaelis-Menten plot of imipenem hydrolysis by ImiS in 50 mM Tris, pH 7.0, at 25 C. The data were fitted to Michaelis-Menten equation with uncompetitive substrate inhibition (26).

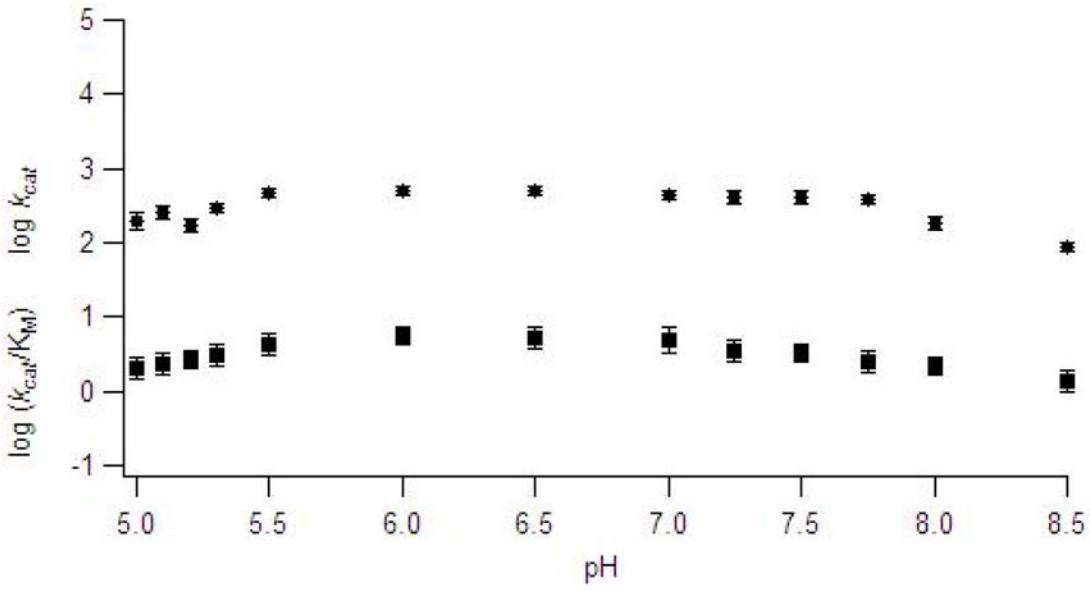

Figure 2.

pH Dependence plots of log k_{cat} (●) and log k_{cat}/K_M(▪) for the hydrolysis of imipenem by ImiS in MTEN buffer. The data points represent average values from at least 3 trials. Error bars represent standard deviation of multiple trials.

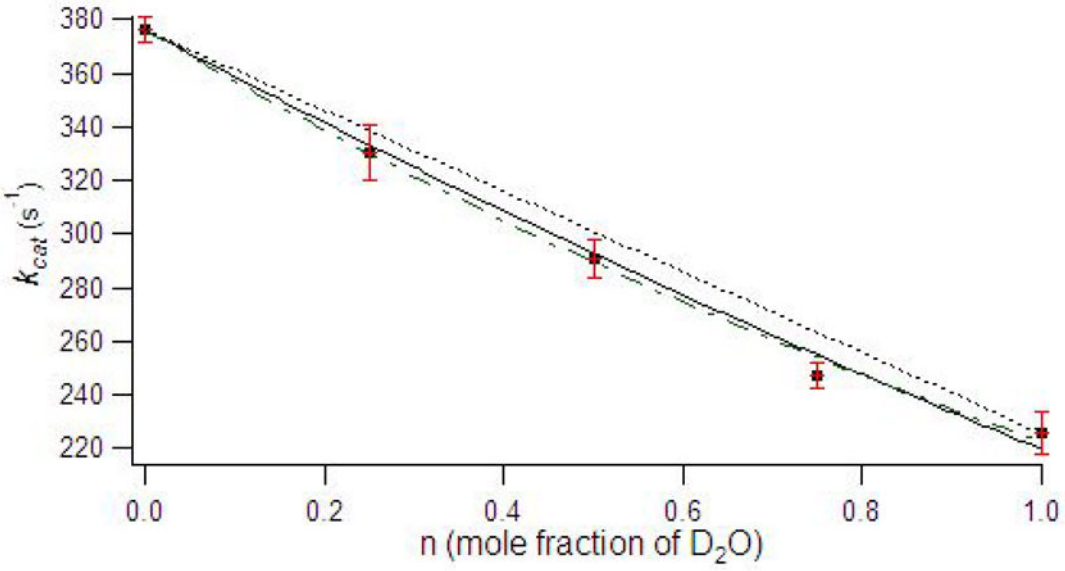

Figure 3.

Proton inventory of imipenem hydrolysis by ImiS. Data points represent averages of at least 3 trials, and error bars are standard deviations. The data were fitted to single proton (dotted line), two proton (solid line), and multiple proton in flight (dash–dot) models (30).

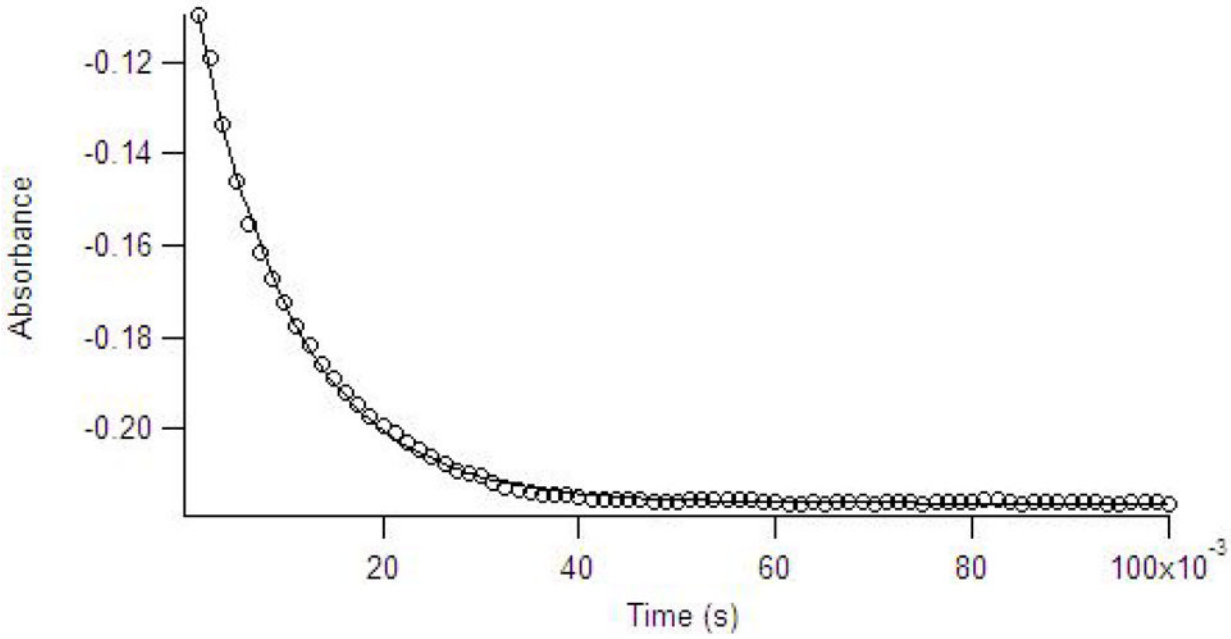

Figure 4.

Stopped-flow UV-Vis data (data points) collected at 300 nm for the reaction of 120 μM ImiS with 100 μM imipenem in 50 mM Tris buffer, pH 7.0, at 2 °C. The solid line is the simulated progress curve generated by KINSIM when using the kinetic mechanism in Scheme 1 and the rate constants in Table 2.

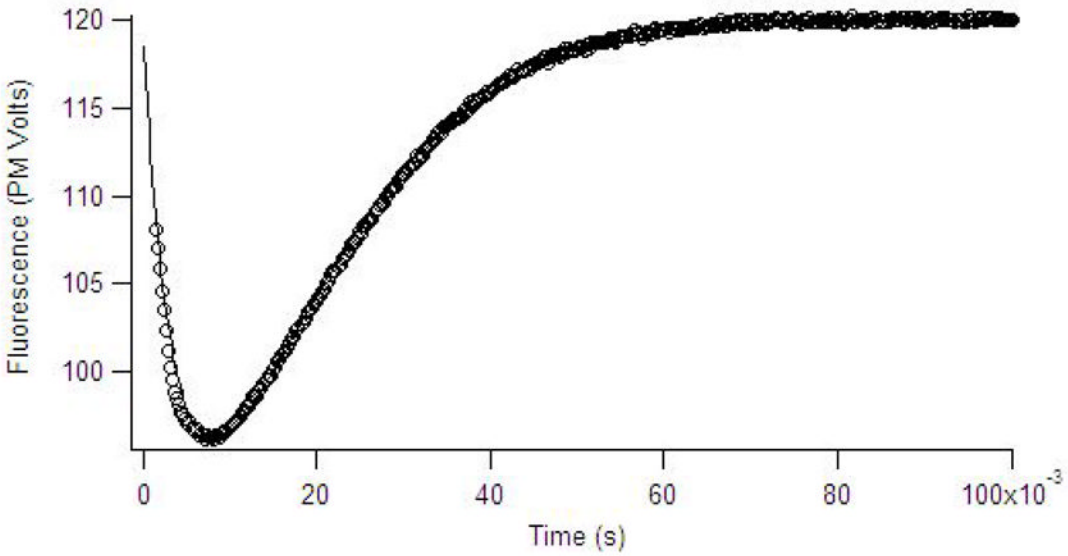

Figure 5.

Stopped-flow fluorescence data (data points) of 120 μM of ImiS reacted with 100 μM imipenem in 50 mM Tris, pH 7.0, at 2 °C. The data points show time dependence of the fluorescence emission at 320 nm after excitation at 280 nm. The solid line is the simulated progress curve generated by KINSIM when using the kinetic mechanism in Scheme 1 and the rate constants in Table 2.

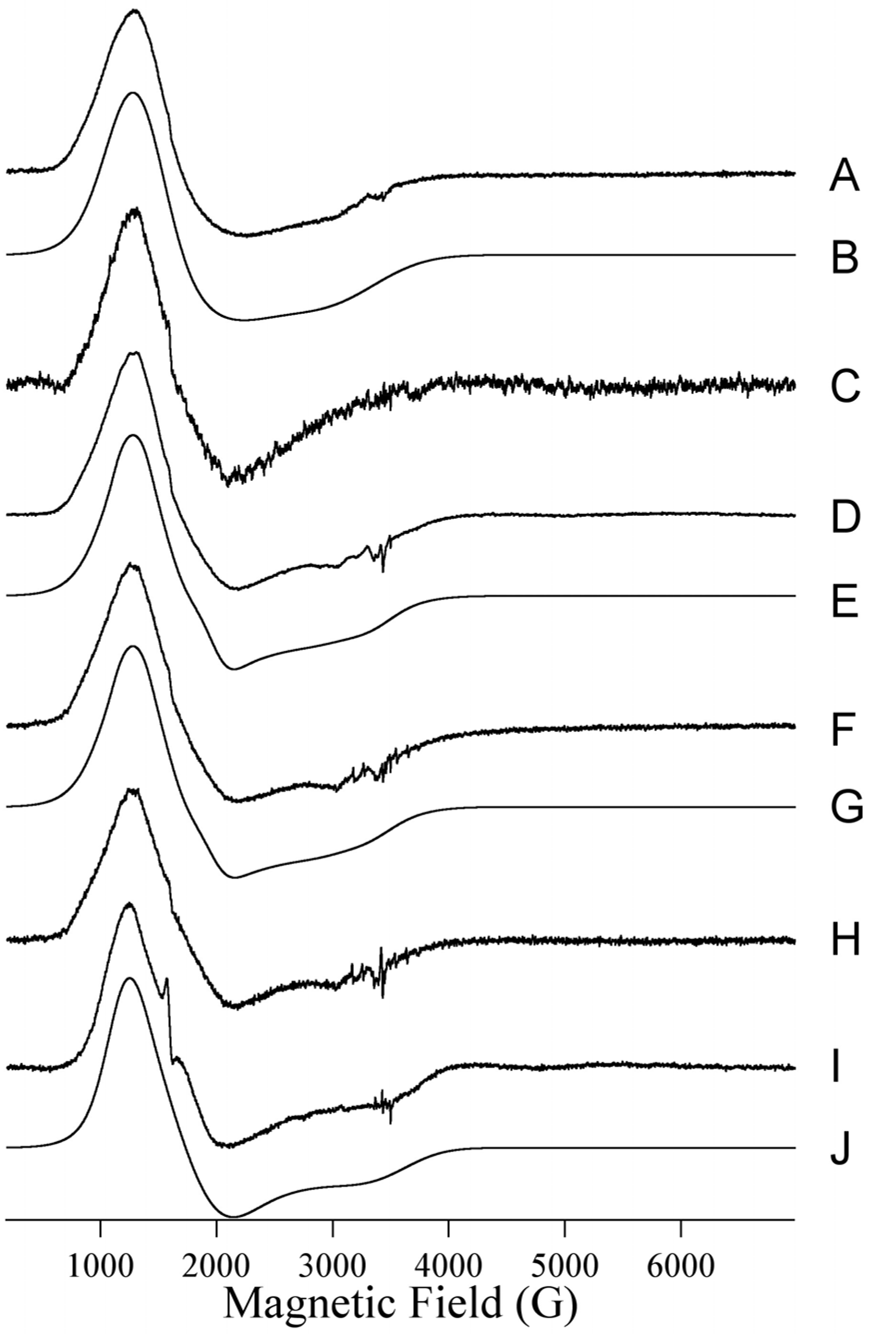

Figure 6.

Trace A shows the resting EPR signal of Co(II)-substituted ImiS. Initial concentrations of ImiS and imipenem were 1 and 5 mM, respectively. Traces C, D, F, H, and I show the EPR spectra of Co(II)-substituted ImiS upon reaction with imipenem for 10 ms at 2 °C (C), 21 ms at 2 C (D), 32 ms at 2 °C (F), 73 ms at 2 °C (H), and 2 s at 2 °C (I). Trace B is a computer simulation of (A) assuming $S = 3/2$, $M_S = |\pm 1/2\rangle$, $g_{x,y} = 2.25$, $g_z = 2.31$, $E/D = 0.076$. Traces E, G, and J are models for D, F, and I, respectively, and consist of (0.94 × A) + (0.06 × Trace C of Figure 7) (E), (0.89 × A) + (0.11 × Trace C of Figure 7)(F), and (0.45 × A) + (0.65 × Trace C of Figure 7) (I). Experimental EPR spectra were recorded at 12 K with 1 mW microwave power at 9.63 GHz. 10 G (mT) field modulation at 100 KHz was employed.

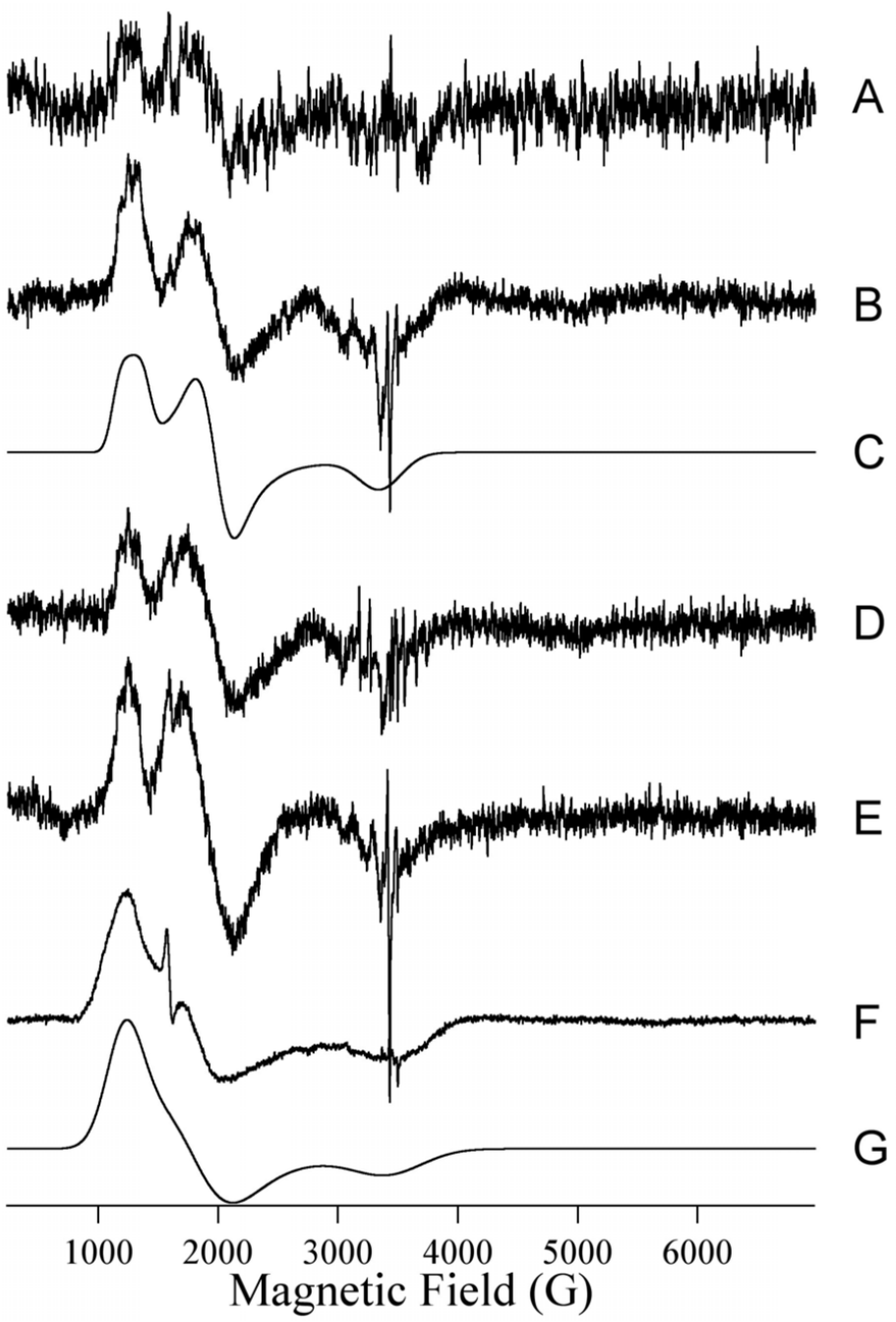

Figure 7.

Isolated species. Traces A, B, D, E and F are the EPR difference spectra generated by subtraction of the resting signal (Trace A of Fig. 6) from those of ImiS upon reaction with imipenem at 2 °C for 10 ms, 21 ms, 32 ms, 73 ms and 2 seconds, respectively. Traces C and G are the computer simulations of (B) and (F) assuming $S = 3/2$, $M_S = |\pm 1/2\rangle$, $g_{x,y} = 2.24$, $g_z = 2.18$, $E/D = 0.145$, $A_y(^{59}\text{Co}) = 40$ G, and $S = 3/2$, $M_S = |\pm 1/2\rangle$, $g_{x,y} = 2.35$, $g_z = 2.12$, $E/D = 0.13$.

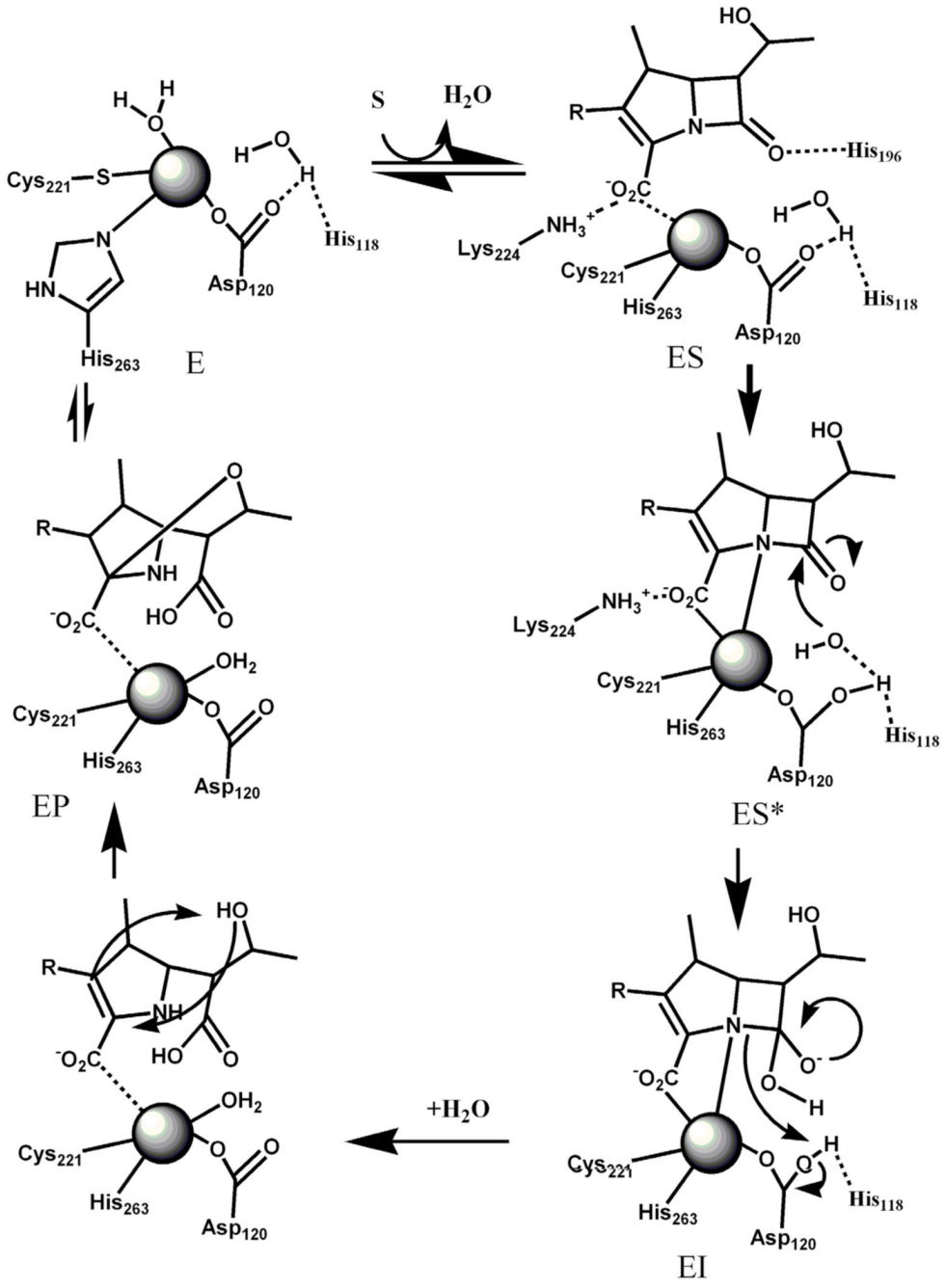

Figure 8.
Proposed reaction mechanism for ImiS.

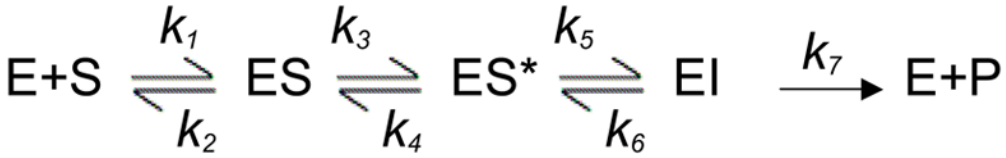

Scheme 1.

Table 1

Steady-state kinetic constants and metal content of ImiS mutants[a].

Enzyme	Imipenem k_{cat} (s^{-1})	Imipenem K_m (μM)	Meropenem k_{cat} (s^{-1})	Meropenem K_m (μM)	Zn(II) eq.As-isolated	Zn(II) eq. Zn(II)-loaded[b]
Wild-type	350 ± 15	100 ± 10	296 ± 20	308 ± 55	0.90 ± 0.06	0.85 ± 0.06
K224T	17 ± 3	208 ± 90	0.67 ± 0.07	136 ± 30	0.80 ± 0.07	0.78 ± 0.15
N233S	303 ± 27	109 ± 22	270 ± 28	151 ± 33	0.77 ± 0.08	0.90 ± 0.08

[a] Steady-state kinetic constants and metal content were determined on at least 3 different preparations of the enzymes. Steady-state kinetic studies were conducted in 50 mM Tris, pH 7.0, at 25 °C.

[b] Zn(II)-loaded samples were prepared by incubating the as-isolated enzymes with 100 μM Zn(II) for 30 minutes and dialyzed 3 times versus 1L of 50 mM Tris, pH 7.0, for 2 hours each.

Biochemistry. Author manuscript; available in PMC 2008 December 8.

TABLE 2

Results of global fitting analysis of stopped-flow fluorescence data to Scheme 1

Parameter	fitted rate
k_1 ($M^{-1}s^{-1}$)	$1.0 \times 10^{8} \pm 1.0 \times 10^{-3}$
k_2 (s^{-1})	$1.0 \times 10^{4} \pm 1.0 \times 10^{-3}$
k_3 (s^{-1})	990 ± 1
k_4 (s^{-1})	$2.4 \times 10^{-4} \pm 8.6 \times 10^{-7}$
k_5 (s^{-1})	163 ± 1
k_6 (s^{-1})	$4.0 \times 10^{-3} \pm 1.7 \times 10^{-6}$
k_7 (s^{-1})	98 ± 1

Substrate used in the stopped-flow studies was imipenem. Data were fitted with Applied Photophysics PC ProK global fitting software using the mechanism in Scheme 1. The reported uncertainties represent standard errors as determined by the ProK software (non-linear Marquardt-Levenberg algorithm).